Relevance of alcoholic solvents in the growth of ZnO nanoparticles and ZnO hierarchical nanorod structures on their optical and opto-electrical properties

Keshav Nagpal, Erwan Rauwel, Frederique Ducroquet, Isabelle Gélard, Protima Rauwel

Article title

Relevance of alcoholic solvents in the growth of ZnO nanoparticles and ZnO hierarchical nanorod structures on their optical and opto-electrical properties.

Keshav Nagpal[a], Erwan Rauwel[a], Frederique Ducroquet[b], Isabelle Gélard[c], Protima Rauwel[a]*

[a]Institute of Forestry and Engineering, Estonian University of Life Science, Kreutzwaldi 56/1, Tartu, Estonia

[b]Université Grenoble Alpes, IMEP-LaHC, 38016 Grenoble, France

[c] Université Grenoble Alpes, CNRS, Grenoble INP, LMGP, F-38000 Grenoble, France

Corresponding author: Protima Rauwel, protima.rauwel@emu.ee

Received xxxxxx
Accepted for publication xxxxxx
Published xxxxxx

Abstract

We report on the synthesis of ZnO nanoparticles and ZnO hierarchical nanorod structures using four different alcohols i.e., methanol, isopropanol, ethanol, and aqueous ethanol (70% alcohol, 30% water). The syntheses of the nanoparticles were carried out by non-aqueous and hydrothermal routes. In general, absolute alcohol allows a better control of the synthesis reaction and nanoparticles as small as 5 nm were obtained, confirmed by TEM. XPS analysis elucidated the chemical states that were correlated to the synthesis reaction. For the nanorod growth, these four alcohols were used as seeding solvents, followed by hydrothermal ZnO nanorod growth. Here, the seed layer tailored the nanorod diameters and surface defects, which were studied by SEM and photoluminescence spectroscopy. Subsequently, The ZnO nanorods were electrically characterized and exhibited persistent photoconductivity under UV irradiation of 365nm. The differences in conductivity in dark and under UV irradiation were attributed to the size of the nanorods, defect states, semiconductor band bending and oxygen adsorption-desorption mechanisms. Parameters such as photoresponse and photosensitivity are also calculated in order to evaluate their applicability in UV sensors. This work demonstrates optimization of the physical, chemical, electrical and optical properties of both ZnO nanostructures via the use of alcoholic solvents.

Keywords: ZnO, nanoparticles, nanorods, band bending, depletion region, sol-gel, photoresponse, persistent photoconductivity

1. Introduction

Metal-oxide-semiconductor nanostructures are suitable candidates for optoelectronic devices, such as chemical sensors, solar cells, ultra-violet (UV) lasers, UV photodetectors, as well as visible and UV light emitting diodes [1-4]. Among them, the intrinsic n-type ZnO semiconductor has attracted interest due to its wide band gap of 3.37 eV, high excitation binding energy of 60 meV, chemical stability and remarkable electrical and optical properties at the nanoscale [5]. However today, the major obstacle in obtaining a ZnO p-n homojunction diode lies in the difficulty of stabilizing a p-type ZnO semiconductor [6].

The physical and chemical properties of ZnO depend on the synthesis conditions that in turn, control the morphology and defect states of the material. In sol-gel synthesis of ZnO, the polar property and the nature of the organic solvent govern the reaction kinetics that subsequently affect the nucleation and growth of ZnO nanostructures [7]. Also, the presence of water in alcoholic solvents accelerates the growth process, leading to a non-uniform morphology of the nanostructures [8,9]. In contrast, using absolute alcohol produces spherically shaped nanoparticles (<10 nm) with a uniform size distribution, thus allowing a better control of the reaction kinetics [10]. In general, the synthesis temperature with absolute alcohol solvents is usually restricted to the boiling point of the solvents. For example, the high boiling point of diethylene glycol (DEG) allows synthesis up to temperatures of 245°C [11,12]. Moreover, the high dielectric constant of polyol solvents results in a quick dissolution of the inorganic zinc precursors. Besides, ZnO nanoparticles harbor large amounts of surface defects owing to their higher surface-to-volume ratio identified using photoluminescence spectroscopy [13-15].

Other than nanoparticles, ZnO can also be grown as hierarchical structures, such as nanorods that tend to exhibit persistent photoconductivity (PPC) in which, the photo-induced current persists even after the removal of UV radiation [16]. In that regard, PPC widens ZnO-nanorod's applicability to photocapacitors for charge storage applications [16-18]. In fact, PPC is attributed to charge trapping at the various defect states within the band gap of ZnO that in turn, retards the decay of the photocurrent [19]. Studies also demonstrate that adsorption-desorption kinetics of surface oxygen play an important role in the ZnO-nanorod conductivity and PPC [17,20]. Furthermore, ZnO-nanorod growth methods include chemical vapor growth, electrochemical deposition and vapor-liquid-vapor growth. Nevertheless, hydrothermal synthesis allows cost-effective and low temperature growth of ZnO nanorods. Various substrates, including silicon, sapphire, polystyrene, polyethylene and indium tin oxide (ITO) coated on glass have been utilized for the growth of ZnO nanorods by hydrothermal synthesis [21-23]. Preliminary seeding on a substrate is a crucial step towards creating ZnO nucleation sites in order to promote a high-density growth of ZnO nanorods. Additionally, factors viz., surface roughness, seeding buffer solution and thickness of the seed layer, tailor the morphology of ZnO nanorods [24].

In this work, four types of alcoholic solvents i.e., methanol, ethanol, isopropanol and aqueous ethanol were used for the sol-gel synthesis of ZnO nanoparticles and for the preparation of the seed layer solution to create nucleation sites for ZnO nanorod growth. Depending upon the dimensionality of the ZnO nanostructure i.e., 0D or 1D, the surface defects varied due to the change in the aspect ratio and consequently, the surface-to-volume ratio. In addition, the solvents of the seed layer also alter defects in the nanorod, which in turn, affect the electrical conductivity and PPC. In order to obtain uniform ZnO nanorod growth, techniques such as chemical vapor deposition and radio frequency magnetron sputtering have been mainly applied for the nucleation of the seeding layer [25,26]. However, in this study a drop-cast method with the help of a micropipette was employed. This technique is cost-effective and allowed to compare the effect of different alcoholic solvents used for seeding on the uniformity of the ZnO-nanorod growth. Therefore, this study provides new perspectives on the solvent-dependent growth of ZnO nanorods. Subsequently, photoluminescence spectroscopy was used to elucidate the various defects present in these nanoparticles and nanorods. Both, the nanoparticles and nanorods were evaluated by physical and chemical characterization techniques. The nanorods were further evaluated for their current *vs* voltage (I-V) characteristics and photoconductivity under UV irradiation.

2. Materials and methods

2.1 Synthesis of ZnO nanoparticles

$Zn(CH_3COO)_2.2H_2O$ (99.9%, Aldrich) was used as a zinc precursor for the synthesis of ZnO nanoparticles via sol-gel routes. Sodium hydroxide (NaOH) (99.9%, Aldrich) was used as an oxidizing agent. All the chemicals used were of analytical grade. In order to prepare 0.05 M solutions of zinc precursor, 219.5 mg of $Zn(CH_3COO)_2.2H_2O$ was dissolved in 20 ml of absolute methanol, aqueous ethanol (70% alcohol, 30% water), absolute ethanol and absolute isopropanol. The zinc precursor solutions were placed in a water bath maintained at 60°C, 65°C, 65°C and 70°C, respectively, controlled by a temperature probe, under continuous magnetic stirring until the zinc salt was completely dissolved in the alcoholic solvent. The temperature was kept below the boiling point of the alcohol in order to prevent its evaporation. In order to dissolve the zinc precursor in isopropanol, the solution was sonicated for 5 minutes after 10 minutes of magnetic stirring at 70°C, after which the solution was again magnetically stirred in a water bath at 70°C. Further, solutions of 0.10 M NaOH (~80 mg) in 20 ml of absolute methanol, aqueous ethanol, absolute ethanol and absolute isopropanol were prepared. The NaOH solution was added dropwise to the zinc precursor solutions. Thereafter, the mixtures were maintained at their growth temperatures for 2 h, after which, they were cooled to ambient temperature. The resulting solutions containing ZnO nanoparticles were then centrifuged at 4500 rpm for 6 min and dried for 24 h in air at 60°C. This resulted in an agglomeration of ZnO nanoparticles in the form of a white pellet that was thereafter crushed in a very fine powder.

2.2 Synthesis of ZnO nanorods

2.2.1 Growth of nanorods

For the growth of ZnO nanorods, ITO coated on a glass substrate was etched at its center for 3 minutes using 12M HCL (Honeywell). Copper tape was used to protect the rest of the ITO surface from etching and also to limit the width of the etched zone to ~4 mm, as shown in Fig. 1. After etching, the copper tape was removed and the etched substrates were cleaned in acetone, isopropanol and DI water with 10 minutes of sonication in each solvent.

2.2.2 Seeding

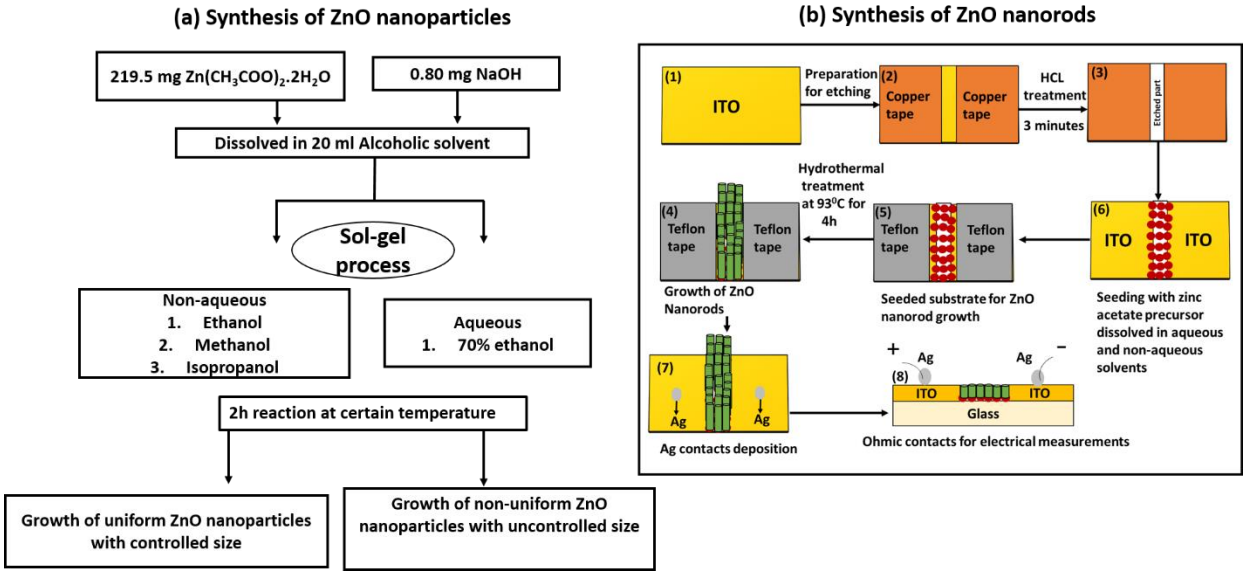

Fig. 1. (a) Schematic for controlled nanoparticle synthesis. (b)) Schematic of the process followed for the seeding and hydrothermal synthesis of ZnO nanorods, (7) silver paste deposition on ITO for ohmic contacts and (8) schematic of the cross-sectional view of the device with ohmic contacts.

In the first step, four seeding solutions were prepared by dissolving 0.011g of $Zn(CH_3COO)_2.2H_2O$ in 10 ml of absolute methanol, aqueous ethanol, absolute ethanol and absolute isopropanol. Similar to ZnO nanoparticle synthesis, the seeding solutions were maintained in a water bath at 60°C, 65°C, 65°C and 70°C under continuous magnetic stirring until the zinc salt was completely dissolved in absolute methanol, aqueous ethanol, absolute ethanol and absolute isopropanol, respectively. After cooling the seeding solutions, 2 µl of the solution was drop-cast on the etched ITO maintained at 60°C on a hot plate. The drop-casting procedure was repeated 25 times for a total of 50 µl of the seeding solution. Thereafter, the seeded ITO was washed with the corresponding solvent and immediately transferred for annealing at 275°C on a hot plate for 15 minutes. Then after cooling down the seeded substrate, the non-seeded part of the ITO was covered with Teflon tape to prevent the growth of ZnO nanorods on the non-seeded part as shown in Fig. 1(b5).

2.2.3 Growth of nanorods

Following the seed layer deposition, the nanorod growth was carried out with 0.595 g of zinc nitrate hexahydrate ($Zn(NO_3)_2.6H_2O$) dissolved in 40 ml of de-ionized water. The solution was magnetically stirred at room temperature for 30 minutes. Thereafter, 0.28 g of hexamethylenetetramine ($(CH_2)_6N_4$, HMTA) was added to the solution under constant magnetic stirring for another 30 minutes. The seeded ITO substrate covered with Teflon tape was then inverted and immersed in the prepared growth solution in a beaker that was

then placed in a Teflon autoclave and sealed tightly. The autoclave was then maintained at 93°C in an oven for 4 h. After which, the autoclave was removed from the oven and cooled down to room temperature. After cooling, the Teflon tape was removed and substrate was thoroughly washed with de-ionized water and dried in an oven maintained at 55°C for 24 h. For electrical measurements of these nanorods, Ag paste was deposited on each side of the ITO heated on a hot plate at 80^0C for 5 minutes as shown in Fig. 1(b7).

2.3 Characterization

X-ray diffraction patterns were collected in Bragg-Brentano geometry using a Bruker D8 Discover diffractometer (Bruker AXS, Germany) with CuKα1 radiation (λ = 0.15406 nm) selected by a Ge (111) monochromator and LynxEye detector. For ZnO nanoparticles prepared using methanol, ethanol and isopropanol, transmission electron microscopy (TEM) was carried out on a Tecnai G2 F20 (Netherlands) field emission gun (FEG) at an acceleration voltage of 200kV with a point-

to-point resolution of 2.4 Å. For the ZnO nanoparticle sample prepared using aqueous ethanol, TEM was carried out on a JEOL 2010 LaB_6 (Jeol, Japan) instrument, operating at 200 kV in TEM mode and providing a point-to-point resolution of 1.9 Å. SEM was carried out on ZEISS EVO MA15 SEM (ZEISS, Germany) in secondary electron mode and a FEI QUANTA 250 environmental SEM FEG operating at 15 kV. XPS measurements were performed at room temperature with a SPECS PHOIBOS 150 hemispherical analyzer (SPECS GmbH, Berlin, Germany) in a base pressure of $5x10^{-10}$ mbar using monochromatic Al K-alpha radiation (1486.74 eV) as an excitation source operated at 300W. The energy resolution as measured by the FWHM of the Ag 3d5/2 peak for a sputtered silver foil was 0.62 eV. The spectra were calibrated relative to the C1s at 284.8eV. The optical absorbance of ZnO nanoparticles and ZnO nanorods were determined using an UV-Vis UV-1600PC spectrophotometer (VWR, US) in the 300–700 nm region. The band gap of ZnO nanoparticles and ZnO nanorods were subsequently calculated with Tauc plots. PL spectroscopy was carried out at room temperature on powder samples with an excitation wavelength of 365 nm of LSM-365A LED (Ocean insight, USA) with a specified output power of 10 mW. The emission was collected by FLAME ES UV-Vis spectrometer (Ocean optics, USA) with spectral resolution of 1.34 nm. Raman spectra were collected using a WITec Confocal Raman Microscope System alpha 300R (WITec Inc., Ulm, Germany). Excitation in confocal Raman microscopy is generated by a frequency-doubled Nd:YAG laser (New-port, Irvine, CA, USA) at a wavelength of 532 nm, with 50 mW maximum laser output power in a single longitudinal mode. The system was equipped with a Nikon (Otawara, Japan) objective with a X20 magnification and a numerical aperture NA = 0.46. The acquisition time of a single spectrum was set to 0.5 s. For electrical measurements, ZnO nanorods were grown on 20mm x 15mm sized unpatterened ITO glass substrates (OSSILA, UK) with 100 nm ITO thickness and 20 Ω/square resistance. The electrical measurements were carried out using two source measure units (Agilent 4156). The measurements were performed by considering ohmic contacts as shown in Fig. 1(h). For the photoresponse of ZnO nanorods, a 125 W Hg lamp with an output wavelength of 365 nm was collected by an optical fiber of diameter 4 mm. The irradiance at the outlet of the optical fiber was measured as ~ 15 mW/cm^2.

3. Results

Table 1 provides the list of ZnO nanoparticles and ZnO nanorod samples synthesized in this work. Samples ZnO-Met, ZnO-Et_{aq}, ZnO-Et and ZnO-Iso refer to ZnO nanoparticles prepared by using absolute methanol, aqueous ethanol, absolute ethanol and absolute isopropanol as solvents. Whereas, samples ZnO NR-Met, ZnO NR-Et_{aq}, ZnO NR-Et and ZnO NR-Iso refer to ZnO nanorod samples prepared by using the same solvents for the seed-layer solution. In this work, terms ZnO samples refer to all ZnO nanoparticle samples and ZnO nanorod samples refer to all ZnO nanorod samples.

Sample	Type	Solvent	Seeding solvent
ZnO-Met	Nanoparticles	Methanol	----
ZnO-Et_{aq}	Nanoparticles	aqueous ethanol	----
ZnO-Et	Nanoparticles	Ethanol	----
ZnO-Iso	Nanoparticles	Isopropanol	----
ZnO NR-Met	Nanorods	----	Methanol
ZnO NR-Et_{aq}	Nanorods	----	aqueous ethanol
ZnO NR-Et	Nanorods	----	Ethanol
ZnO NR-Iso	Nanorods	----	Isopropan-ol

Table. 1. List of abbreviations and solvents used for the as-synthesized ZnO nanoparticles and ZnO nanorods.

3.1 Structure and morphology

XRD patterns of ZnO-Met, ZnO-Et_{aq}, ZnO-Et and ZnO-Iso are shown in Fig. 2(a). The peaks (100), (002), (101), (102), and (110) correspond to the hexagonal Wurtzite structure (a = 3.25 Å and c = 5.20 Å) of ZnO (JCPDS, Card Number 36-1451). Reflections indicating other phases than Wurtzite ZnO are absent in samples ZnO-Met, ZnO-Et_{aq} and ZnO-Et. However, the XRD pattern of sample ZnO-Iso consists of crystalline ZnO nanoparticles of very small sizes. Also, the majority of the additional peaks are related to the zinc acetate precursor (marked 1), others to NaOH (marked 2) and Na metal (marked 3) [27-29]. In fact, for sol-gel synthesis, the reaction time is a crucial parameter for the successful precipitation of crystalline ZnO, which was fixed to 2h for all four types of ZnO nanoparticles in this study. Hu et al. demonstrated the formation of highly crystalline ZnO in a long carbon chain solvent medium of 1-butanol (C_4H_9OH) with a longer reaction times of 11h to 24h [27]. In our study, due to the longer carbon chain of isopropanol (C_3H_7OH) compared to ethanol (C_2H_5OH) and methanol (CH_3OH), the reaction time of 2h was clearly not sufficient for the complete reaction of $Zn(CH_3COO)_2.2H_2O$ with NaOH. In addition, NaOH has a low solubility in isopropyl alcohol, which implies that $Zn(CH_3COO)_2.2H_2O$ and NaOH were unable to fully dissolve and react, leading to the presence of by-products, such as unreacted precursors in the ZnO nanopowder. In the XRD patterns, the indexed peaks for samples ZnO-Met and ZnO-Et and for sample ZnO-Iso are broad compared to sample ZnO-Et_{aq}. An estimation of the average size of the nanoparticles was carried out by using

the full-width-half maximum value in the Scherrer equation (given below) of reflections of ZnO-Met, ZnO-Et and ZnO-Iso.

$$D = \frac{0.9\lambda}{\beta \cos\theta}$$

where D is particle size, λ (= 0.15406 nm) is the wavelength of incident X-ray beam, β is FWHM in radians and θ is Bragg's diffraction angle. The size calculations were carried out using high index reflections (100) and (002) for samples ZnO-Met, ZnO-Et and ZnO-Et_{aq} and (100) and (101) reflection for ZnO-Iso. Average nanoparticle diameters of 10 nm, 9 nm and 7.3 nm were obtained, respectively.

XRD patterns of ZnO NR-Et, ZnO NR-Met, ZnO NR-Et_{aq} and ZnO NR-Iso and ITO are shown in Fig. 2(b). The XRD characteristic peaks (100), (002) and (101) confirm the hexagonal wurtzite structure of ZnO, while the sharp peak at ~34.5^0, which is the out-of-plane reflection, suggests that nanorods grow along the c-axis [30]. The XRD peaks (222) and (400) correspond to ITO coated on glass and are marked (*) in Fig. 2(b) [31]. More detailed information about the particle sizes and shapes of the nanoparticles, as well as the diameters of nanorods were obtained via TEM and SEM analyses, described in the following sections.

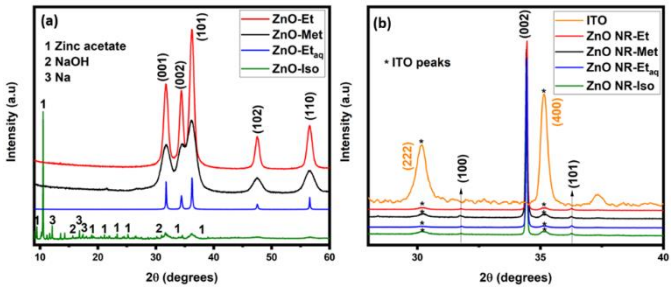

Fig. 2. (a) XRD spectra of samples ZnO-Et, ZnO-Met, ZnO-Et_{aq} and ZnO-Iso. (b) XRD spectra of the ITO substrate (reference) and samples ZnO NR-Et, ZnO NR-Met, ZnO NR-Et_{aq} and ZnO NR-Iso.

The morphology and nanoparticle size of the ZnO samples were studied by TEM, as shown in Fig. 3(a)-3(f). For samples ZnO-Met, ZnO-Et and ZnO-Iso in Fig. 3(a)-3(c), the TEM micrographs reveal spherical nanoparticles with a uniform size distribution. However, the nanoparticles of samples ZnO-Met and ZnO-Et tend to agglomerate (Fig. 3(a) and 3(b)). Size distribution histograms of samples reveal an average size of ~ 4.8 nm, ~5.2 nm and 4.2 nm for samples ZnO-Met, ZnO-Et and ZnO-Iso, respectively. The nanoparticles of the ZnO-Iso sample are monodispersed, which is likely due to the presence of isopropyl groups ($(CH3)_2CHO$) and other unreacted precursors. Additionally, the low magnification image of ZnO-Iso (Fig. 3(e)) provides an overview of the nanoparticles. The needle-like structures of low contrast are the unreacted precursor with dark dots corresponding to ZnO nanoparticles magnified in Fig. 3(c). These organic ligands probably act as a surfactant and prevent ZnO-nanoparticle agglomeration. The HRTEM image of the ZnO-Iso nanoparticles in Fig.3(f) provides a point-to-point resolution of a highly crystalline nanoparticle, thus confirming the XRD result of small and crystalline nanoparticles. Sample ZnO-Et_{aq} (Fig. 3(d)) shows needle-like and hexagonally shaped nanoparticles. In a previous study, the effect of varying the NaOH molar ratio on the morphology of ZnO nanoparticles with an aqueous ethanol solvent was investigated [8]. The authors demonstrated that reaction kinetics leading to the growth of ZnO nanoparticles are accelerated by increasing quantities of OH^- ions in the solution. The increase in hydroxyl ions stimulates the selective and directional growth of nanoparticles, into needle-like structures as well as other irregularly shaped nanoparticles. This suggested that the reaction kinetics are difficult to control in the presence of water. Samples ZnO-Met, ZnO-Et and ZnO-Iso are synthesized with absolute alcohol solvents that are devoid of water and therefore, the reaction rate is slower, which supports the formation of spherically shaped nanoparticles. On the other hand, in the presence of water molecules, the reaction kinetics are quicker, which results in anomalously shaped nanoparticles for sample ZnO-Et_{aq} of Fig. 3(d). ZnO crystal with a growth direction perpendicular to the [0001] basal planes, contains eight facets. The facets at the 2 ends along are polar, while the other six facets forming the sides of the hexagon are non-polar. More precisely, the ZnO crystal lattice has characteristic polar planes (0001) and $(000\bar{1})$ packed with zinc ions (Zn^{2+}) or oxygen ions (O^{2-}), as well as six non-polar planes belonging to a family of planes $[\bar{1}100]$, containing both O and Zn ions making them electrically neutral. ZnO polar planes are highly reactive, and are more likely to participate in the chemical reaction of the ZnO nanorod growth process. In addition, one polar plane anchors the nanorod to the substrate, while the other one is exposed to air i.e., (0001), which is Zn-terminated. Furthermore, in ZnO, the growth rate of individual crystallographic planes is determined by the principle of energy minimization according to which, the growth rate of (0001) plane is the highest and of $(000\bar{1})$ plane is the lowest [32]. Therefore, vertical growth along (0001) direction is the most energetically favorable growth axis, which therefore leads to the rod-shaped growth of ZnO. The largest exposed area of the nanorod in the solution corresponds to the non-

SEM was performed to study the morphology and distribution of the nanorods on the substrates. SEM images from Figs. 3(g)-3(n) are the top view of ZnO nanorod samples. The low magnification SEM images in Figs. 3(g)-3(j), exhibit zones that are devoid of nanorods, indicating discontinuities in the nanorod layer. Figure S3 provides additional SEM images depicting the morphology of the nanorods. In Fig. 3(g), sample ZnO NR-Met exhibits a more

uniform nanorod growth compared to sample ZnO NR-Et and sample ZnO NR-Iso that contain zones devoid of nanorods in Figs. 3(i) and 3(j). Similarly, sample ZnO NR-Et_{aq} exhibits a non-uniform growth with numerous empty areas (Fig. 3(h)). Higher magnification images taken with a titled substrate of the ZnO-nanorod samples in Fig. 3(k)-3(n) exhibit nanorods with diameters listed in table 2. The diameters of ZnO NR-Met, ZnO NR-Et and ZnO NR-Iso samples are similar ~80-90 nm, obtained from size distribution histograms, most likely due to the absence of water in the seeding solutions. Whereas, due to the presence of 30% water in the seeding solution of the ZnO NR-Et_{aq} sample, the nanorod diameter is the largest (~110 nm), among the four samples. All nanorod samples present hexagonally facetted nanorods, as visible in figure 3 (k-n). In fact, a hexagonally facetted polar surfaces, necessary to minimize the energy requirement during growth. In addition, the presence of HMTA during the synthesis process reduces the ZnO growth in the radial direction by restricting it along non-polar m-planes (diametrically) and by favoring the growth in the direction of polar c-planes (longitudinally) [32]. In fact, HMTA also covers the surfaces of the non-polar sidewalls with OH groups, similar to a surfactant, whereby it reduces the radial growth of the nanorods [33]. HMTA is a pH buffer that ensures continuous growth of the ZnO nanorod and at the same time regulates the release of OH^- ions. In addition,

the concentration of HMTA in the reaction mixture also modifies the nucleation process by interacting with the ZnO

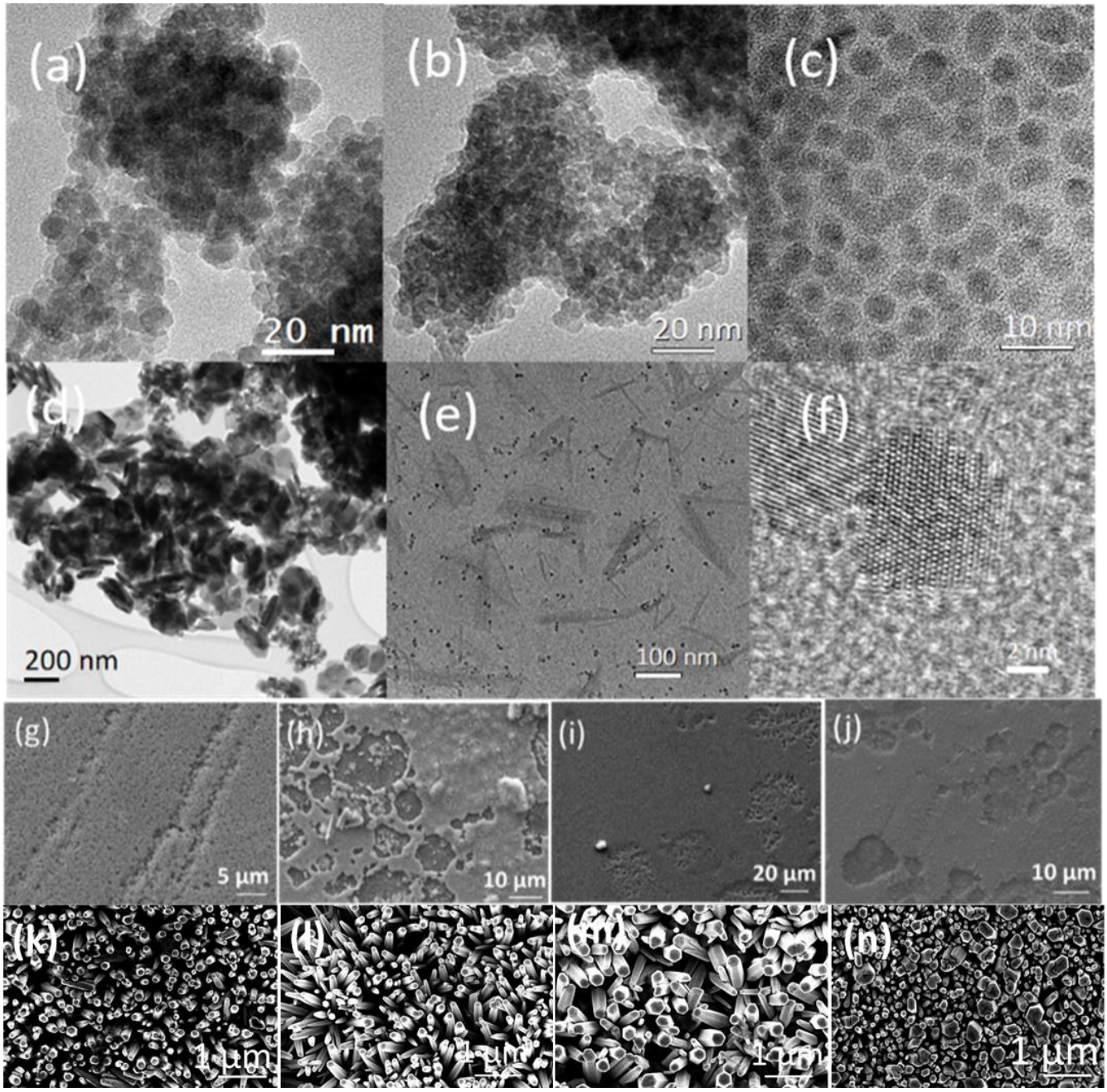

Fig. 3. High magnification TEM micrographs of samples (a) ZnO-Met, (b) ZnO-E_t, (c) ZnO-Iso and (d) ZnO-Et_{aq}, (e) low magnification TEM image of ZnO-Iso, (f) HRTEM image of single highly crystalline ZnO-Iso nanoparticle. Low magnification SEM images of samples (g) ZnO NR-Met, (h) ZnO NR-Et_{aq}, (i) ZnO NR-Et and (j) ZnO NR-Iso, showing the surface morphology. Higher magnification SEM images of samples in titled mode (k) ZnO NR-Met, (l) ZnO NR-Et_{aq}, (m) ZnO NR-Et and (n) ZnO NR-Iso, showing hexagonally facetted morphology and density of ZnO nanorods.

seed layer, thus increasing the density of ZnO nanorods [34].

Sample	Particle size (XRD)	Particle size (TEM)	Nanorod diameter (SEM)
ZnO-Met	10 nm	4.8 nm	----
ZnO-Et_{aq}	----	----	----
ZnO-Et	9 nm	5.2 nm	----
ZnO-Iso	7.3 nm	4.2 nm	----
ZnO NR-Met	----	----	85 nm
ZnO NR-Et_{aq}	----	----	110 nm
ZnO NR-Et	----	----	90 nm
ZnO NR-Iso	----	----	80 nm

Table. 2. List of average particle size of ZnO nanoparticle samples obtained from XRD, and TEM, and average diameter of ZnO nanorods obtained from XRD and SEM. Size distribution histograms are provided in S1 and S2 for nanoparticles and nanorods, respectively.

The high-resolution XPS spectra of the C1s and O1s regions of the samples ZnO-Met, ZnO-Et_{aq}, ZnO-Et and ZnO-Iso are shown in Fig. 4 and Fig. 5, respectively. The C-C bond at 284.8 eV in the C1s spectra (Fig. 4), corresponds to adventitious carbon [35]. The bonds C-OH, O=C-O present in these samples are contributions from the NaOH and zinc acetate precursor used during the synthesis [10]. Therefore, C1s spectra confirm the presence of chemisorbed OH groups on the surface of the nanoparticles. The C1s spectrum of sample ZnO-Iso manifests the highest contributions from the O=C-O, C-OH and C=O bonds, which confirm the presence of unreacted zinc acetate precursor and NaOH on the surface ZnO-Iso nanoparticles. Due to the long carbon chain of isopropanol, the dissolution of $Zn(CH_3COO)_2.2H_2O$ salt in isopropanol is very slow and isopropyl groups can anchor easily on the surface of ZnO through oxygen bonding, whereby lowering its solubility. In the case of the other solvents and under similar conditions, $Zn(CH_3COO)_2.2H_2O$ salt dissolution is quicker as the solvent does not anchor on the ZnO nanoparticle surface. This explains the lower contributions from the O=C-O, C-OH and C=O bonds in the case of ZnO-Met and ZnO-Et samples. On the other hand, for sample ZnO-Et_{aq}, due the presence of water, the dissolution of the $Zn(CH_3COO)_2.2H_2O$ salt and thus the nucleation rate are the quickest and therefore, the sample shows the lowest contributions from O=C-O, C-OH and C=O bonds. In addition, the presence of water contributes to by-product and surfactant removal from the surface of ZnO nanoparticles [13].

The high resolution O1s spectra of samples ZnO-Met, ZnO-Et_{aq}, ZnO-Et and ZnO-Iso are shown in Fig. 5. The main peak is lattice oxygen (Zn-O) bond at ~529 eV for all samples that is characteristics of ZnO nanoparticles. Additionally, for all samples the peak at ~531.5 eV corresponds to the presence of hydroxyl groups that are bonded to the ZnO nanoparticle surface. However, this peak

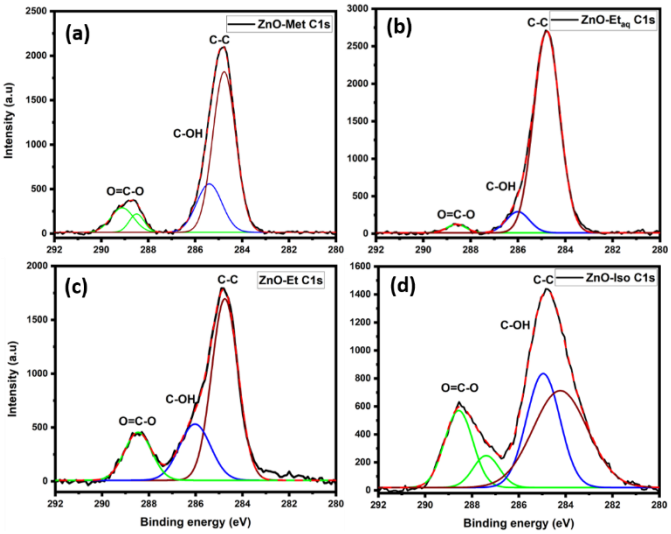

Fig. 4. C1s XPS spectra of samples (a) ZnO-Met, (b) ZnO-Et_{aq}, (c) ZnO-Et and (d) ZnO-Iso.

can also be related to oxygen defects or surface oxygen vacancies [36]. TEM analysis highlighted the very small size of nanoparticles, supporting the presence of surface oxygen vacancies and C1s spectra indicated that hydroxyl groups are anchored on the nanoparticle surface. For samples ZnO-Met, ZnO-Et_{aq} and ZnO-Et, O1s peak structure is similar with only differences in relative intensities of the peaks, implying a comparable surface chemistry. A noticeable difference is the relative increase of the Zn-OH peak to the lattice oxygen peak, which increases with the absolute alcohol chain length. For sample ZnO-Iso, the intensity for the Zn-OH peak is higher than the lattice Zn-O peak, indicating a higher amount of adsorbed OH groups and unreacted Zn precursor. The presence of Na or NaOH is illustrated by the peak at 536 eV in Fig. 5(d), also confirmed by XRD [37]. Therefore, chemical states of ZnO-Iso obtained from C1s and O1s spectra suggest that the surface of sample ZnO-Iso is covered with isopropyl groups from isopropanol, acetate groups from the Zn precursor, and hydroxyl groups from NaOH. Additionally, the Zn 2p spectra are provided in S4. For the ZnO-Iso sample, this further highlights the presence of another phase of Zn with +2 oxidation states at lower binding

energies [38]. In our case, the peak at binding energy of ~ 1018 eV is most likely related to the unreacted Zn acetate precursor.

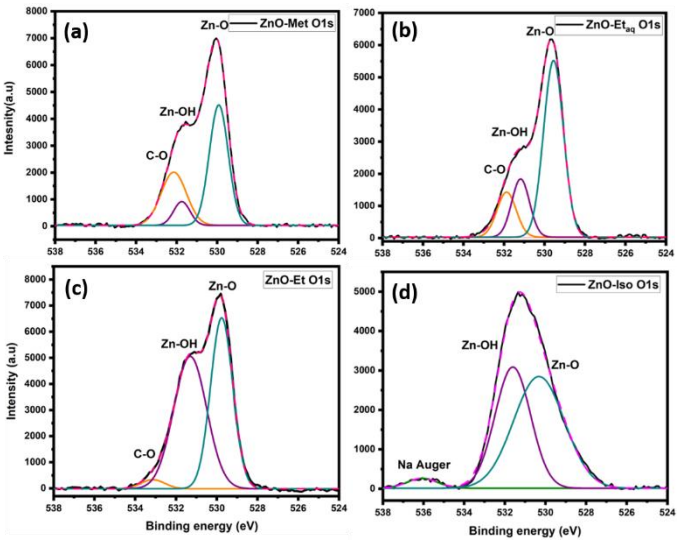

Fig. 5. O1s XPS spectra of samples (a) ZnO-Met, (b) ZnO-Et_{aq}, (c) ZnO-Et and (d) ZnO-Iso.

The vibrational modes of the ZnO nanoparticles were investigated using Raman spectroscopy. In Fig. 6, the Raman spectra compare the different vibrational modes from these samples in the range of 100-800 cm^{-1}. The modes visible at ~440 cm^{-1}, ~585 cm^{-1} and ~667 cm^{-1} correspond to E_{2H}, E_1 (LO) and E_2 (TO) modes, respectively and are known as first-order phonon modes. The modes visible at ~320 cm^{-1} and 506 cm^{-1} correspond to the E_{2H}–E_{2L} and $E_1(TO)$ + E_{2L} modes and are known as multiphonon scattering modes [39,40]. In particular, the E_{2H} mode at 440 cm^{-1} corresponds to lattice-oxygen or Zn-O vibrations and confirms the formation of ZnO. Whereas, the mode E_1 (LO) corresponds to oxygen-related defects [10]. In general, the modes below 300 cm^{-1} are Zn-related defects, while the modes above 300 cm^{-1} are related
to oxygen or both, zinc- and oxygen-related complex defects [41]. Sample ZnO-Et shows the highest intensity of E_{2H} mode relative to samples ZnO-Et_{aq} and ZnO-Met. Whereas, for sample ZnO-Iso, the E_{2H} mode has largely diminished. Several factors affect the peak shifts and their intensities, including the presence of secondary phases and inorganic contaminants that modify the phonon confinement of the nanoparticle. Besides, XRD and TEM clearly indicate the presence of very small nanoparticles that are embedded in organic compounds. The latter most likely dampens this particular phonon mode. Further, the high Na:Zn ratio obtained from XPS of 1.5:1 suggests that the presence of Na and NaOH could affect this mode. For e.g., the Raman study of ZnO-CdO based nanocomposite has shown a similar decrease in the E_{2H} mode of ZnO suggesting that the presence of CdO modifies the phonon confinement of ZnO [42]. Additionally, the E_1(TO) band indicates a breakdown in long range ordering in ZnO and the E_1(LO) band suggests the

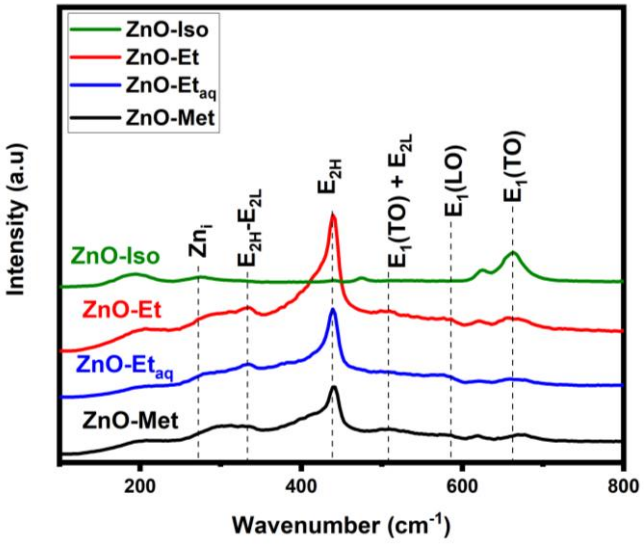

Fig. 6. Raman spectra of samples ZnO-Iso, ZnO-Et, ZnO-Et_{aq}, and ZnO-Met.

presence of oxygen vacancies and zinc interstitials or complex defects combining both [43]. The ratio of intensities of E_{2H} and E_1(LO) therefore indicates that ZnO-Et has the lowest amount of oxygen vacancies.

3.2 Optical properties

The band gaps of the as-synthesized ZnO-nanoparticle samples and ZnO-nanorod samples were calculated via UV-Vis absorption spectroscopy followed by Tauc plots presented in Fig. 7(a) and 7(b), respectively. The band gaps of the ZnO nanoparticles range from 3.11-3.28 eV, and for ZnO nanorod samples are ~3.1-3.2 eV. All these values are within the range of the theoretical band gap of ZnO [44]. The absorption spectra of both, ZnO nanoparticle and nanorod samples revealed a sharp shoulder at 3.3 eV stretching down to 2 eV, shown in S5. However, shoulders related to defect level absorption in the visible region were absent.

The typical PL spectra of ZnO nanoparticles consisting of near band edge emission (NBE) and defect level emission (DLE) are presented in Fig. 7(c) without normalization, as the quantities of nanoparticle for each sample used for PL analysis were identical ~5 mg. In fact, an influence of the solvent medium on the intensities of the DLE is clearly observed. For example, sample ZnO-Et exhibits the highest DLE compared to sample ZnO-Et_{aq} that emits the least intense NBE, owing to
the absence of water in the former. The origin of the DLE is attributed to the combination of several point defects, such as V_O, V_{Zn}, O_i, Zn_i, and their complexes [45,46]. Whereas, the NBE emission originates from the recombination of excitons

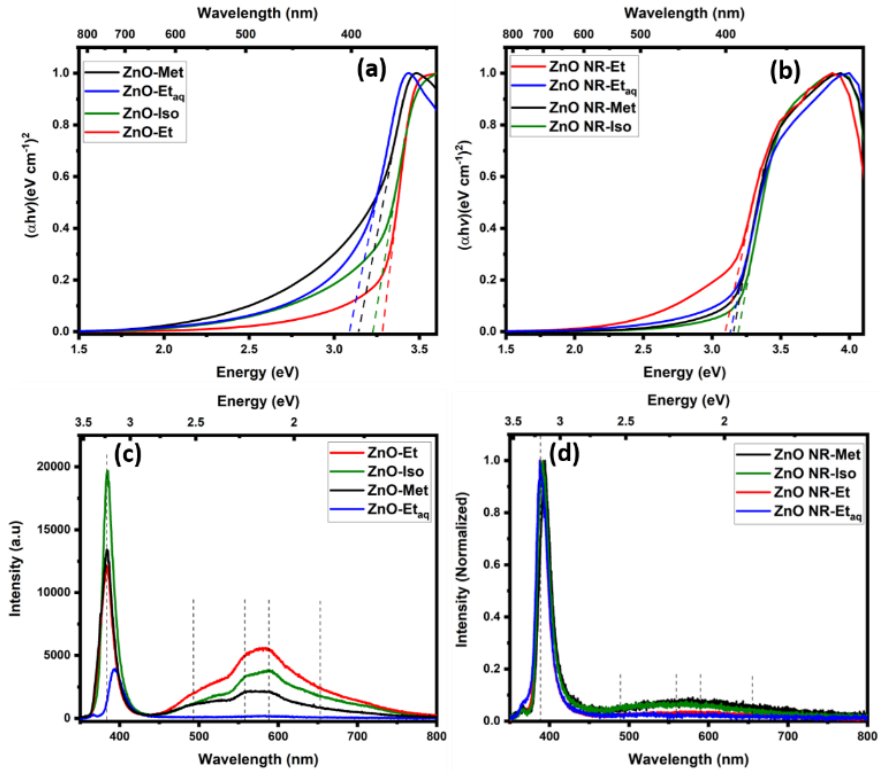

Fig. 7. Tauc plot of samples (a) ZnO-Met, ZnO-Et$_{aq}$, ZnO-Et and ZnO-Iso and (b) ZnO NR-Met, ZnO NR-Et$_{aq}$, ZnO NR-Et, and ZnO NR-Iso, (c) PL spectra of samples ZnO-Met, ZnO-Et, ZnO-Et$_{aq}$ and ZnO-Iso and (d) normalized PL spectra of samples ZnO NR-Met, ZnO NR-Et, ZnO NR-Et$_{aq}$ and ZnO NR-Iso.

due to band-to-band transitions [8]. Moreover, the ratio of NBE-to-DLE is indicative of the crystalline quality of the sample. In the case of the ZnO-Et$_{aq}$ sample, the NBE-to-DLE ratio is the highest, indicating the best crystalline quality. The high crystalline quality is attributed to the presence of water in the synthesis mixture that provides an oxidizing environment during ZnO nanoparticle growth, encouraging the precipitation of larger nanoparticles with lower quantities of surface defects. However, the NBE is slightly redshifted compared to the other samples, suggesting the presence of shallow donor states in the sample. Since, this sample also has the largest nanoparticles or the lowest surface-to-volume ratio, it therefore explains the negligible DLE that is surface-related.

On the other hand, samples synthesized with pure ethanol, methanol and isopropanol exhibited a lower NBE-to-DLE ratio, with the lowest for sample ZnO-Et. The increase in DLE for these samples is indicative of surface defects such as Vo^{++} i.e., surface-related oxygen vacancies at 2.2 eV [47]. Additionally, their very small particle size (~5 nm) enhances the DLE. The 2.2 eV transition is associated with the capture of a surface-trapped holes by V_O^{+} to form V_O^{++}. Eventually, an electron from the conduction band can recombine with V_O^{++} to subsequently emit at 2.2 eV. The singly ionized oxygen vacancy V_O^{+} or volume oxygen vacancy emits at ~2.5 eV. Both types of vacancies produce green photoluminescence in ZnO. In nanoparticles of size ~5 nm, quantities Vo^{+} are negligible compared to Vo^{++}.

Furthermore, the intensity of the green emission can be strongly influenced by chemisorbed species on the surface, especially for nanoparticles with very small sizes. Since PL measurements were performed in air, hydroxyl groups or oxygen molecules are adsorbed on the surface of the nanoparticles, creating a depletion region. The chemisorbed oxygen species induce an upward band bending in the as-synthesized ZnO nanoparticles, which allows V_O^{++} to convert into V_O^{+} through the capture of an electron or oxygen radicals from the surface-depletion region [10,48]. Therefore, the observed dominant green emission in ZnO-Met, ZnO-Et and ZnO-Iso samples is mainly surface related with differences in their relative intensities. The rather intense DLE of sample ZnO-Iso suggests that the unreacted precursors and isopropyl groups do not passivate the surface defects.

The PL spectra of ZnO nanorod samples consisting of NBE and DLE are shown in the Fig. 7(d). Here, the spectra were normalized in order to emphasize on the negligible defect level emission and secondly because the nanorod surface was not uniform for all the samples. Compared to the ZnO nanoparticle samples, the ZnO-nanorod samples show

higher NBE-to-DLE ratio and therefore, harbor lower intrinsic defects. However, for samples ZnO NR-Met and ZnO NR-Iso, there is a hint of DLE suggesting a higher amount of surface defects, despite their nanorod diameters being similar to ZnO NR-Et. The NBE of the ZnO nanorod samples are between 388-393 nm and correspond to the transitions from Zn shallow donor levels to the valence band. Apart from the NBE, two of the ZnO-nanorod samples also show DLE of low intensity, which is a combination of point defects including, V_O, V_{zn}, O_i, and Zn_i, similar to the ZnO nanoparticles. The growth solution for the ZnO nanorod samples was prepared using DI water as a solvent i.e., in oxygen-rich conditions that reduces the number of oxygen-related defects in the ZnO-nanorod samples. In particular, the major DLE components of the nanorod and nanoparticle samples, regardless of their relative intensities, are yellow-green (~2.2 eV and ~2.5 eV), orange-red (~2.1 eV) and red (~1.95 eV). The yellow-orange emission at ~2.1 eV is due to the transitions from Zn_i to O_i. Whereas, the red emission at ~1.95 eV is attributed to the transitions related to Zn_i, usually observed in oxygen-rich conditions [49].

3.3 Electrical and optoelectrical properties of ZnO nanorods

In Fig. 8(a), the I-V characteristics of the ZnO nanorod samples at room temperature are obtained in dark and under UV light in the range from -3V to +3V. For all the ZnO nanorod samples, the I-V characteristics are ohmic with differences in the output currents. The overall output currents in decreasing order of magnitude were for ZnO NR-Met, ZnO NR-Et, ZnO NR-Iso, ZnO NR-Et_{aq}. Factors that affect the conductivity, include the presence of defects, as well as the uniformity of the nanorod layer. In the SEM images of Fig. 2(g)-2(m), the ZnO NR-Met nanorod layer was the most continuous followed by ZnO NR-Et nanorod and ZnO NR-Iso. Finally, ZnO NR-Et_{aq} was the least continuous and its surface
revealed a large number of voids, which is the plausible explanation for the lowest output current, among all the nanorod samples. The I-V characteristics of ZnO-nanorod samples were also evaluated under UV light. The general tendency under UV radiation indicated a higher output current compared to dark conditions.

Fig. 8(b) is the current *vs* time (I-t) curves of ZnO nanorod samples at a constant bias of 3V, measured in dark. The conductivity of ZnO nanorods depends on the surface defects and the amount of oxygen adsorbed on the surface of ZnO nanorods, as oxygen plays an important role in the surface charge transport mechanism of ZnO nanorods [50,51]. In fact, in dark conditions, an oxygen molecule is adsorbed on the surface of ZnO nanorods, resulting in an upward band bending and a depletion region of oxygen radicals is created at the nanorod surface, as illustrated in Fig. 8(c) and (d). With time, the adsorption of oxygen radicals increases, leading to trapping or storing of electrons at the depletion

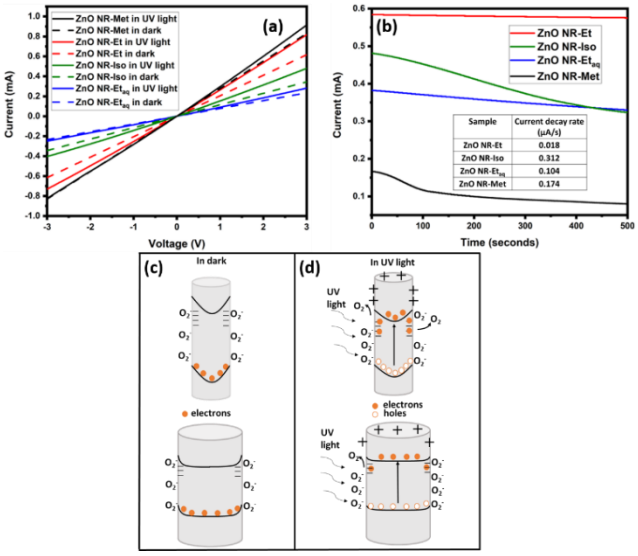

Fig. 8. (a) I-V characteristics of ZnO nanorod samples taken in dark (dashed line) and UV light (solid line) from -3V to +3V, (b) I-t characteristics of ZnO nanorod samples taken in dark at a constant bias of 3V. The inset in (b) is calculations of current decay rate (μA/s). Schematic of the band bending and oxygen-ion adsorption-desorption mechanisms of smaller and larger nanorods in (c) dark and (d) UV

region, which in turn, results in the reduction of ZnO nanorod conductivity [52,53]. The phenomenon of trapping is all the more pronounced when surface defects are present. In Fig. 8(b), all the ZnO nanorod samples exhibit a reduction in the conductivity as a result of charge trapping over time. Both, ZnO NR-Met followed by sample ZnO NR-Iso show a 2-step decrease in current due to high charge trapping. The first step of current decrease is more abrupt and is attributed to the rapid filling of surface traps. Once the majority of the trap states are filled, a second slope appears, which corresponds to a more gradual filling of the remaining trap states that eventually should lead to a steady-state current. The defect states in these samples shown in the PL emission spectra of Fig. 7, consist of Zn_i or V_O, especially for samples ZnO NR-Met and ZnO NR-Iso that contribute to electron trapping and consequently, lower the conductivity over time in these samples. On the other hand, the decay rates of the current in sample ZnO-Et and ZnO-Et_{aq} in the inset of fig. 8(b), are much lower owing to a lower amount of surface defects. Besides, the nanorod diameter also plays an important role in terms of charge trapping. As illustrated in Fig. 8(c), a larger diameter nanorod will tend to have a smaller depletion region and consequently, a lower overall band banding. Additionally, a larger nanorod harbors lower number of surface defects due to the smaller surface-to-

volume ratio. Therefore, the decrease in the current due to charge trapping is less dominant for ZnO NR-Et_{aq} [54]. On the other hand, even though the diameter of ZnO-Et is comparable to ZnO-Iso and ZnO-Met, it displays the lowest current decay of 0.018 μA/s, which is mostly related to the negligible amount of surface defects leading to lower charge trapping.

times at intervals of 10 s each, with possible errors of 2 s due to manual operation. For all the samples, the current obtained during the UV on-cycle shows an increase of 15%-25% for all cycles. In fact, under UV radiation, holes are generated in the valence band due to excitation and transfer of electrons to the conduction band, which in turn, reduce the overall band bending, along with the width of the depletion region as

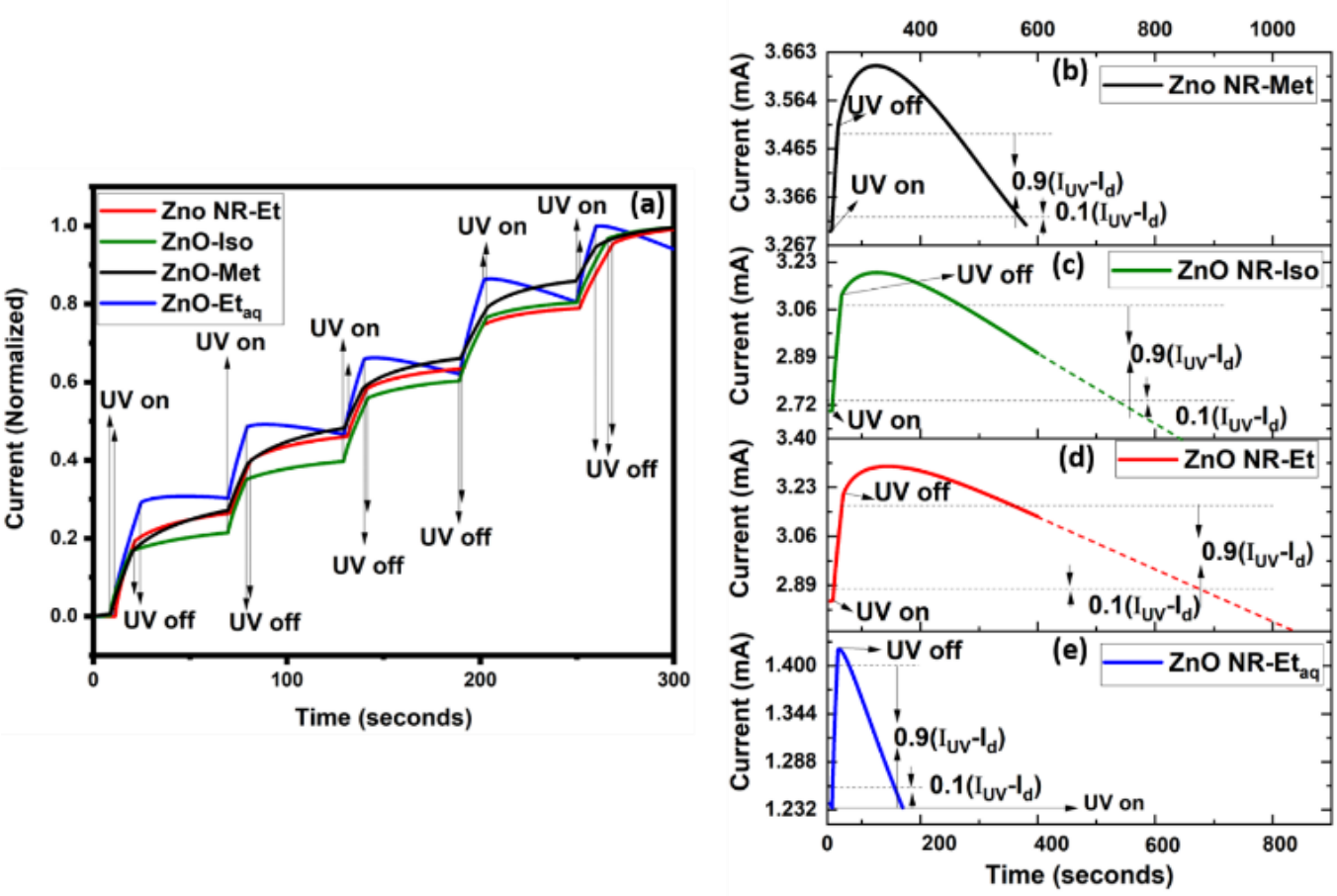

Fig. 9. (a) I-t characteristics of ZnO nanorod samples under UV on-off cycles with total measurement for 300 seconds at a constant bias of 3V. Single on-off cycle of samples (b) ZnO NR-Met, (c) ZnO NR-Iso, (d) ZnO NR-Et and (e) ZnO NR-Et_{aq} at a constant bias of 3V. The dashed line in Fig. (c) and (d) are the extrapolations of the decay to the X-intercept.

Under UV light, Saxena et al. demonstrated a higher photocurrent in vacuum than in air from ZnO microstructures. Similarly, their current decay time in dark was found to be higher in vacuum than in air [55]. Furthermore, Bao et al. studied the photoconductivity of ZnO nanowires in vacuum by radiating the ZnO nanowire with three different power sources of UV radiation for 5 h, until saturation photocurrent was reached. Subsequently, the sample was left in vacuum for another 12 h during which, the current maintained a steady state. Upon release of the vacuum, an immediate and abrupt decay of the current was observed [17]. In this study, several on-off cycles of UV radiation were examined in order to evaluate the photoresponse of each sample. The UV light was turned on 5

shown in Fig. 8(d). Nevertheless, due to the remnant upward band bending of ZnO, some holes are still accumulated on the surface. Simultaneously, some of the electrons are trapped at the surface of the nanorods, while others travel to the volume of the nanorod and contribute to the conductivity. The surface accumulated holes subsequently combine with the adsorbed oxygen radicals that then desorb from the ZnO nanoparticle surface in the form of oxygen molecules. Once again for larger nanorods, the oxygen-desorption mechanism is less dominant with regards to the conductivity. After each UV on-cycle, samples were maintained in dark for 50 seconds, during which an increase in the upward band bending and in turn, to a decrease in the current were observed. Ideally, the current should drop to its dark current

value [56]; however, the dark current recovery depends on the rate at which photoexcited carriers recombine, which depends on the size of the depletion region, as illustrated in Fig. 8 (c) and(d). The larger the depletion region, the slower the recombination rate, which results in a slow decay of current that persists even in dark. In general, the size of the depletion region is inversely proportional to the presence of surface defects and can be corroborated to PL results. PPC was observed during the UV off-cycles (50 seconds) for all samples, during which the current did not drop to its initial value. In fact, PPC is directly related to the surface defects and the oxygen environment around ZnO [57]. For sample ZnO NR-Et_{aq}, a fast decay compared to other samples was observed during UV off-cycles, which can be attributed to the lowest number of surface defects and relatively smaller

depletion region. In addition, ZnO NR-Et, ZnO NR-Met and ZnO NR-Iso exhibit similar PPC behaviors, owing to the similarity in their diameters. Since the nanorod diameter can also affect the conductivity, hence, PPC is more pronounced in samples with smaller nanorod diameters harboring higher amount of surface defects or presenting more pronounced upward band bending. The I-t characteristics of ZnO NR-Et sample at a lower bias of 10 mV for various on-off cycles under UV radiation are provided in figure S6 (a). At a low bias, a low current in the µA range was obtained compared to the high voltage bias of 3V, where output currents were in mA ranges. Therefore, for this study, a 3 V bias was selected, in order to clearly highlight the differences in I-t characteristics. In addition, we measured I-t characteristics of sample ZnO NR-Etaq for a long on- cycle interval of ~500 seconds to attain current saturation under UV radiation. The result is shown in supplementary figure S6 (b). However, the current did not reach saturation in 500s. Therefore, short intervals of ~10-12 seconds were employed to study I-t characteristics under UV radiation for various on-off cycles, in this present study.

The properties of the nanorods for UV sensor applications were assessed using the responsivity, sensitivity and response time [58], as shown in Fig. 9(b)-9(e). ZnO nanorod samples were irradiated with UV light at different on-off intervals ($\tau_{uv\text{-}light}$), as listed in table 3. After UV irradiation, the off cycle lasted for 350 s for all the samples. The I-t curves in Fig. 9(b)-9(e) are plotted for one on-off cycle. Samples ZnO NR-Et_{aq} and ZnO NR-Met reached their dark current within the off-cycle interval. However, for samples ZnO NR-Et and ZnO NR-Iso, the time required to reach the dark current value exceeded the off-cycle interval and was therefore estimated via extrapolation, shown by the dotted line in Fig. 9(c) and 9(d). The sensitivity was determined using the equation: $S = \frac{I_{UV}}{I_{dark}}$, where I_{UV} is the current, when UV radiation is turned off, I_{dark} is the dark current just before switching on UV radiation. The sensitivities are similar for all the nanorod samples i.e., between ~1.1 to 1.5, as listed in table 3. These values suggest that regardless of differences in I_{dark} and total UV-radiation time ($\tau_{uv\text{-}light}$), the increase of photocurrent with respect to dark current is approximately the same for all

samples. The responsivity (µA/W) was calculated by using the

equation, $R = \frac{I_{UV}-I_{dark}}{P_{in}A_{eff}}$, where P_{in} is the incident UV irradiation power of Hg UV lamp through the optical fiber and A_{eff} is the effective active area of the probe. The highest responsivity was calculated for sample ZnO NR-Iso, followed by samples ZnO NR-Et, ZnO NR-Met and lowest for sample ZnO NR-Et_{aq} (table 3). The response time has two parameters i.e., the rise time (τ_{rise}), which is the amount of time required for the ZnO nanorod samples to reach 90% from 10% of the current under UV-radiation. On the other hand, τ_{decay} is the amount of time required for the current to decay from 90% to 10% once the UV radiation is turned off. The τ_{rise} is directly dependent on the total UV radiation time i.e., $\tau_{uv\text{-}light,}$ listed in table 3. On the other hand, τ_{decay} is an intrinsic property of the samples and depends on surface defects, oxygen adsorption and band bending of the sample. Furthermore, τ_{decay} is the parameter that provides information on the photoresponse or UV sensor applicability of the samples. Once the UV radiation is turned off, two phenomena are likely to occur. The first phenomenon is related to charge de-trapping, which causes a rapid increase in current before its decay after switching off the UV radiation. In samples ZnO NR-Met, ZnO NR-Iso and ZnO NR-Et, an increase in the current reaching a peak value before decay is observed, owing to charge de-trapping [52,56]. The second phenomenon is related to PPC observed

Table. 3. List of parameters calculated from the I-t characteristics of UV on off cycle (Fig. 11(b)-11(e)).

Sample	Sensitivity	Responsivity (mA/W)	τ_{rise} (s)	I_{rise} rate (µA/s)	τ_{decay} (s)	I_{decay} rate (µA/s)	$\tau_{uv\text{-}light}$ (s)
ZnO NR-Met	1.067	116.8	8.4	20.5	107.5	1.6	10.9
ZnO NR-Iso	1.153	220.2	13.3	25.3	264.4	1.29	14.8
ZnO NR-Et	1.129	193.7	14.2	20.2	318.1	0.92	17.3
ZnO NR-Et_{aq}	1.145	95.5	7.9	18	77.8	1.84	11.6

in all the samples due to which the τ_{decay} takes over 70 s to descend to dark current values [56]. Additionally, PPC without charge de-trapping is only observed in ZnO NR-Et_{aq}. Also, τ_{decay} was estimated by the extrapolation to ~320 s for sample ZnO NR-Et and to ~265 s for sample ZnO NR-Iso. The τ_{decay} was slowest for sample ZnO NR-Et, which suggests that persistent conductivity is the most dominant in this sample. The second fastest τ_{decay} (~110 seconds) was calculated for sample ZnO NR-Met and the fastest τ_{decay} of ~80 s was calculated for sample ZnO NR-Et_{aq}. Since, sample ZnO NR-Et_{aq} shows an immediate decay in current after turning off the UV radiation, it has potential as a UV detector with low heating effects owing to low charge trapping.

The sensitivity, responsivity and rise-decay time are affected by growth conditions, applied bias, power of the UV source and the presence of plasmonic nanoparticles. Several works on the UV responsivity and sensitivity of ZnO nanorods are available. The applied bias was as high as 5V in certain studies [59-61]. For example, Sheikh et al. have obtained a

responsivity of 364.81 A/W, under 365 nm radiation with a flux of 1.8 $\mu W/cm^2$ at 5 V bias [62]. The rise time and decay

time were calculated as 17 seconds and 22 seconds, respectively. Since ammonia was used in the hydrothermal synthesis, N acceptor states could create additional defects that influence the rise and decay time. Plasmonic nanoparticles such as Al also tend to increase the sensitivity of the ZnO nanorod photodetector. For example, compared to bare ZnO nanorods, devices with plasmonic Al nanoparticles show increase in their responsivity from 53 mA/W to 267 mA/W and in their sensitivity from 9.5 to 47.8 under 325 nm UV light (5 mW/cm^2) at 3.0 V bias [63]. In addition, Liu et al. demonstrated that photoresponse of ZnO nanorods can be enhanced by covering it with a polymer such as PMMA. Here, the PMMA itself does not contribute to the UV response as it is UV transparent and electrically insulating, but it helps to enhance the responsivity of ZnO nanorods, by passivating the surface states and hindering oxygen adsorption [64]. In those studies, either the applied bias or the incident flux was higher or the surface of the ZnO nanorods was also passivated. Nevertheless, electrical conductivity of ZnO nanorods depends also on its polarity and crystal orientation and is enhanced for highly directional nanorods that require well-textured seed layers for their growth [65].

4. Conclusion

In this work we have successfully grown ZnO nanoparticles and nanorod seed layers using four different solvents, i.e., methanol, ethanol, isopropanol and aqueous ethanol. The solvents played an important role on the surface defect generation, size and morphology of the nanoparticles and seed layer nucleation. In general, non-aqueous solvents produced spherically shaped nanoparticles of uniform size and allowed a better control of the reaction kinetics. Long chain alcohols tend to produce smaller, more uniform and monodispersed nanoparticles, with the drawback of leaving unreacted products in the final powders. Subsequently, these solvents were also used in the seed layer solutions for nanorod growth. Similar to nanoparticles, the nanorods with absolute alcohol seed layers possessed equivalent sizes, indicating that the seed layer nucleation played an important role in the nanorod diameters. Furthermore, the aqueous ethanol solvent produced larger nanorods, owing to the faster reaction kinetics of the seed layer, in turn, producing larger nucleation sites. Since, the growth of the nanorods was carried out in identical conditions after the seed layer deposition, the differences in the electrical properties can therefore be directly and uniquely linked to the solvent used in the seed layer solution. All the samples presented an ohmic behavior with changes in current output over time that can be directly related to the size of the nanorods, uniformity of the nanorod layer, band bending and surface defects. Under UV illumination, the I-t on-off cycles revealed their potential for UV sensor applications, especially for the ZnO Et_{aq} sample that exhibited the fastest responses for UV on-off cycles. The other samples demonstrated PPC with slow current decay rates in off-cycles in ambient conditions. In fact, PPC is a defect- and ambient-related phenomenon, being sensitive to oxygen in the surrounding. Therefore, PPC can be useful in gas sensing, piezo and biosensing applications. Additionally, manipulating these nanorods under vacuum, would open applications in charge storage devices such as photocapacitors. In general, larger nanorods with fewer defects would serve as UV sensors while as, smaller nanorods demonstrate potential for photocapacitance. In the next step, a hybrid diode-structure will be prepared consisting of these ZnO nanorods and conducting polymers and other applications will be explored.

References

1. Liu, K.; Sakurai, M.; Aono, M. ZnO-Based Ultraviolet Photodetectors. *Sensors* **2010**, *10*, 8604-8634, doi:10.3390/s100908604.
2. Chaudhary, S.; Umar, A.; Bhasin, K.K.; Baskoutas, S. Chemical Sensing Applications of ZnO Nanomaterials. *Materials* **2018**, *11*, 287.
3. Wibowo, A.; Marsudi, M.A.; Amal, M.I.; Ananda, M.B.; Stephanie, R.; Ardy, H.; Diguna, L.J. ZnO nanostructured materials for emerging solar cell applications. *RSC Advances* **2020**, *10*, 42838-42859, doi:10.1039/D0RA07689A.
4. Pearton, S.J.; Ren, F. Advances in ZnO-based materials for light emitting diodes. *Current Opinion*

in Chemical Engineering **2014**, *3*, 51-55, doi:https://doi.org/10.1016/j.coche.2013.11.002.
5. Lin, B.; Fu, Z.; Jia, Y. Green luminescent center in undoped zinc oxide films deposited on silicon substrates. *Applied Physics Letters* **2001**, *79*, 943-945, doi:10.1063/1.1394173.
6. Park, C.H.; Zhang, S.B.; Wei, S.-H. Origin of p-type doping difficulty in ZnO: The impurity perspective. *Physical Review B* **2002**, *66*, 073202, doi:10.1103/PhysRevB.66.073202.
7. Hu, Z.; Oskam, G.; Searson, P.C. Influence of solvent on the growth of ZnO nanoparticles. *Journal of Colloid and Interface Science* **2003**, *263*, 454-460, doi:https://doi.org/10.1016/S0021-9797(03)00205-4.
8. Nagpal, K.; Rapenne, L.; Wragg, D.S.; Rauwel, E.; Rauwel, P. The role of CNT in surface defect passivation and UV emission intensification of ZnO nanoparticles. *Nanomaterials and Nanotechnology* **2022**, *12*, 18479804221079419, doi:10.1177/18479804221079419.
9. Oskam, G.; Soberanis Domínguez, O.E. The Effect of Water on the Nucleation Kinetics of ZnO Nanoparticles. *ECS Transactions* **2006**, *3*, 17, doi:10.1149/1.2357092.
10. Nagpal, K.; Rauwel, E.; Estephan, E.; Soares, M.R.; Rauwel, P. Significance of Hydroxyl Groups on the Optical Properties of ZnO Nanoparticles Combined with CNT and PEDOT:PSS. *Nanomaterials* **2022**, *12*, 3546.
11. Jezequel, D.; Guenot, J.; Jouini, N.; Fievet, F. Preparation and Morphological Characterization of Fine, Spherical, Monodisperse Particles of ZnO. *Materials Science Forum* **1994**, *152-153*, 339-342, doi:10.4028/www.scientific.net/MSF.152-153.339.
12. Poul, L.; Ammar, S.; Jouini, N.; Fievet, F.; Villain, F. Synthesis of Inorganic Compounds (Metal, Oxide and Hydroxide) in Polyol Medium: A Versatile Route Related to the Sol-Gel Process. *Journal of Sol-Gel Science and Technology* **2003**, *26*, 261-265, doi:10.1023/A:1020763402390.
13. Rauwel, E.; Galeckas, A.; Rauwel, P.; Sunding, M.F.; Fjellvåg, H. Precursor-Dependent Blue-Green Photoluminescence Emission of ZnO Nanoparticles. *The Journal of Physical Chemistry C* **2011**, *115*, 25227-25233, doi:10.1021/jp208487v.
14. Ungula, J.; Dejene, B.F. Effect of solvent medium on the structural, morphological and optical properties of ZnO nanoparticles synthesized by the sol–gel method. *Physica B: Condensed Matter* **2016**, *480*, 26-30, doi:https://doi.org/10.1016/j.physb.2015.10.007.
15. Foo, K.L.; Kashif, M.; Hashim, U.; Liu, W.-W. Effect of different solvents on the structural and optical properties of zinc oxide thin films for optoelectronic applications. *Ceramics International* **2014**, *40*, 753-761, doi:https://doi.org/10.1016/j.ceramint.2013.06.065.
16. Bayan, S.; Mohanta, D. ZnO nanorod-based UV photodetection and the role of persistent photoconductivity. *Philosophical Magazine* **2012**, *92*, 3909-3919, doi:10.1080/14786435.2012.698761.
17. Bao, J.; Shalish, I.; Su, Z.; Gurwitz, R.; Capasso, F.; Wang, X.; Ren, Z. Photoinduced oxygen release and persistent photoconductivity in ZnO nanowires. *Nanoscale Research Letters* **2011**, *6*, 404, doi:10.1186/1556-276X-6-404.
18. Altaf, C.T.; Coskun, O.; Kumtepe, A.; Rostas, A.M.; Iatsunskyi, I.; Coy, E.; Erdem, E.; Sankir, M.; Sankir, N.D. Photo-supercapacitors based on nanoscaled ZnO. *Scientific Reports* **2022**, *12*, 11487, doi:10.1038/s41598-022-15180-z.
19. Yadav, H.K.; Sreenivas, K.; Gupta, V. Persistent photoconductivity due to trapping of induced charges in Sn/ZnO thin film based UV photodetector. *Applied Physics Letters* **2010**, *96*, doi:10.1063/1.3427417.
20. Anu Roshini, R.; Nagpal, K.; Senthamarai Kannan, E. Anomalous conductance induced by hydrogen on ZnO and catalyzed ZnO nanoflowers. *Europhysics Letters* **2019**, *127*, 57005, doi:10.1209/0295-5075/127/57005.
21. Saidin, N.U.; Choo, T.F.; Kok, K.Y. Hydrothermal growth of ZnO: a substrate-dependent study on nanostructures formation. *IOP Conference Series: Materials Science and Engineering* **2018**, *298*, 012016, doi:10.1088/1757-899X/298/1/012016.
22. Baruah, S.; Thanachayanont, C.; Dutta, J. Growth of ZnO nanowires on nonwoven polyethylene fibers. *Science and Technology of Advanced Materials* **2008**, *9*, 025009, doi:10.1088/1468-6996/9/2/025009.
23. Park, H.K.; Hong, S.P.; Do, Y.R. Vertical Growth of ZnO Nanorods Prepared on an ITO-Coated Glass Substrate by Hydrothermal-Electrochemical Deposition. *Journal of The Electrochemical Society* **2012**, *159*, D355, doi:10.1149/2.078206jes.
24. Song, J.; Lim, S. Effect of Seed Layer on the Growth of ZnO Nanorods. *The Journal of Physical Chemistry C* **2007**, *111*, 596-600, doi:10.1021/jp0655017.
25. Ong, W.L.; Low, Q.X.; Huang, W.; van Kan, J.A.; Ho, G.W. Patterned growth of vertically-aligned ZnO nanorods on a flexible platform for feasible transparent and conformable electronics applications. *Journal of Materials Chemistry* **2012**, *22*, 8518-8524, doi:10.1039/C2JM00027J.
26. Wang, C.H.; Wong, A.S.W.; Ho, G.W. Facile Solution Route to Vertically Aligned, Selective Growth of ZnO Nanostructure Arrays. *Langmuir* **2007**, *23*, 11960-11963, doi:10.1021/la702296q.
27. Hu, Z.; Escamilla Ramírez, D.J.; Heredia Cervera, B.E.; Oskam, G.; Searson, P.C. Synthesis of ZnO Nanoparticles in 2-Propanol by Reaction with

Water. *The Journal of Physical Chemistry B* **2005**, *109*, 11209-11214, doi:10.1021/jp0506033.
28. Mao, J.; Gu, Q.; Gregory, D.H. Revisiting the Hydrogen Storage Behavior of the Na-O-H System. *Materials* **2015**, *8*, 2191-2203.
29. Stenger, J.; Kwan, E.; Eremin, K.; Speakman, S.; Dan, K.; Heather, S.; Huang, S.; Kennedy, A.; Richard, N.; Narayan, K. LITHOL RED SALTS: CHARACTERIZATION AND DETERIORATION. *E-Preservation Science* **2010**.
30. Zhou, Q.; Wen, J.Z.; Zhao, P.; Anderson, W.A. Synthesis of Vertically-Aligned Zinc Oxide Nanowires and Their Application as a Photocatalyst. *Nanomaterials* **2017**, *7*, 9.
31. Vieira, N.; Fernandes, E.; De Queiroz, A.; Guimarães, F.; Zucolotto, V. Indium tin oxide synthesized by a low cost route as SEGFET pH Sensor. *Materials Research* **2013**, *16*, 1156-1160, doi:10.1590/S1516-14392013005000101.
32. Gerbreders, V.; Krasovska, M.; Sledevskis, E.; Gerbreders, A.; Mihailova, I.; Tamanis, E.; Ogurcovs, A. Hydrothermal synthesis of ZnO nanostructures with controllable morphology change. *CrystEngComm* **2020**, *22*, 1346-1358, doi:10.1039/C9CE01556F.
33. Murillo, G.; Leon-Salguero, E.; Martínez-Alanis, P.R.; Esteve, J.; Alvarado-Rivera, J.; Güell, F. Role of aluminum and HMTA in the hydrothermal synthesis of two-dimensional n-doped ZnO nanosheets. *Nano Energy* **2019**, *60*, 817-826, doi:https://doi.org/10.1016/j.nanoen.2019.04.017.
34. Parize, R.; Garnier, J.; Chaix-Pluchery, O.; Verrier, C.; Appert, E.; Consonni, V. Effects of Hexamethylenetetramine on the Nucleation and Radial Growth of ZnO Nanowires by Chemical Bath Deposition. *The Journal of Physical Chemistry C* **2016**, *120*, 5242-5250, doi:10.1021/acs.jpcc.6b00479.
35. Chen, X.; Wang, X.; Fang, D. A review on C1s XPS-spectra for some kinds of carbon materials. *Fullerenes, Nanotubes and Carbon Nanostructures* **2020**, *28*, 1048-1058, doi:10.1080/1536383X.2020.1794851.
36. Sahai, A.; Goswami, N. Probing the dominance of interstitial oxygen defects in ZnO nanoparticles through structural and optical characterizations. *Ceramics International* **2014**, *40*, 14569-14578, doi:https://doi.org/10.1016/j.ceramint.2014.06.041.
37. Zhao, N.; Li, C.; Guo, X. Long-life Na–O2 batteries with high energy efficiency enabled by electrochemically splitting NaO2 at a low overpotential. *Physical Chemistry Chemical Physics* **2014**, *16*, 15646-15652, doi:10.1039/C4CP01961J.
38. Kumar, P.; Mathpal, M.C.; Inwati, G.K.; Kumar, S.; Duvenhage, M.-M.; Roos, W.D.; Swart, H.C. Study of Defect-Induced Chemical Modifications in Spinel Zinc-Ferrites Nanostructures by In-Depth XPS Investigation. *Magnetochemistry* **2023**, *9*, 20.
39. Sharma, A.; Singh, B.P.; Dhar, S.; Gondorf, A.; Spasova, M. Effect of surface groups on the luminescence property of ZnO nanoparticles synthesized by sol–gel route. *Surface Science* **2012**, *606*, L13-L17, doi:https://doi.org/10.1016/j.susc.2011.09.006.
40. Gao, Q.; Dai, Y.; Li, C.; Yang, L.; Li, X.; Cui, C. Correlation between oxygen vacancies and dopant concentration in Mn-doped ZnO nanoparticles synthesized by co-precipitation technique. *Journal of Alloys and Compounds* **2016**, *684*, 669-676, doi:10.1016/j.jallcom.2016.05.227.
41. Khachadorian, S.; Gillen, R.; Choi, S.; Ton-That, C.; Kliem, A.; Maultzsch, J.; Phillips, M.R.; Hoffmann, A. Effects of annealing on optical and structural properties of zinc oxide nanocrystals. *physica status solidi (b)* **2015**, *252*, 2620-2625, doi:10.1002/pssb.201552453.
42. Reddy, C.V.; Babu, B.; Shim, J. Synthesis, optical properties and efficient photocatalytic activity of CdO/ZnO hybrid nanocomposite. *Journal of Physics and Chemistry of Solids* **2018**, *112*, 20-28, doi:https://doi.org/10.1016/j.jpcs.2017.09.003.
43. Souissi, A.; Amlouk, M.; Khemakhem, H.; Guermazi, S. Deep analysis of Raman spectra of ZnO:Mo and ZnO:In sprayed thin films along with LO and TA+LO bands investigation. *Superlattices and Microstructures* **2016**, *92*, 294-302, doi:https://doi.org/10.1016/j.spmi.2016.02.024.
44. Davis, K.; Yarbrough, R.; Froeschle, M.; White, J.; Rathnayake, H. Band gap engineered zinc oxide nanostructures via a sol–gel synthesis of solvent driven shape-controlled crystal growth. *RSC Advances* **2019**, *9*, 14638-14648, doi:10.1039/C9RA02091H.
45. Alvi, N.H.; ul Hasan, K.; Nur, O.; Willander, M. The origin of the red emission in n-ZnO nanotubes/p-GaN white light emitting diodes. *Nanoscale Research Letters* **2011**, *6*, 130, doi:10.1186/1556-276X-6-130.
46. Kumar Jangir, L.; Kumari, Y.; Kumar, A.; Kumar, M.; Awasthi, K. Investigation of luminescence and structural properties of ZnO nanoparticles, synthesized with different precursors. *Materials Chemistry Frontiers* **2017**, *1*, 1413-1421, doi:10.1039/C7QM00058H.
47. Pramanik, S.; Mondal, S.; Mandal, A.C.; Mukherjee, S.; Das, S.; Ghosh, T.; Nath, R.; Ghosh, M.; Kuiri, P.K. Role of oxygen vacancies on the green photoluminescence of microwave-assisted grown ZnO nanorods. *Journal of Alloys and Compounds* **2020**, *849*, 156684, doi:https://doi.org/10.1016/j.jallcom.2020.156684.
48. Vanheusden, K.; Warren, W.L.; Seager, C.H.; Tallant, D.R.; Voigt, J.A.; Gnade, B.E. Mechanisms behind green photoluminescence in ZnO phosphor powders. *Journal of Applied Physics* **1996**, *79*, 7983-7990, doi:10.1063/1.362349.

49. Przezdziecka, E.; Guziewicz, E.; Jarosz, D.; Snigurenko, D.; Sulich, A.; Sybilski, P.; Jakiela, R.; Paszkowicz, W. Influence of oxygen-rich and zinc-rich conditions on donor and acceptor states and conductivity mechanism of ZnO films grown by ALD—Experimental studies. *Journal of Applied Physics* **2020**, *127*, doi:10.1063/1.5120355.
50. Ke, J.-J.; Liu, Z.-J.; Kang, C.-F.; Lin, S.-J.; He, J.-H. Surface effect on resistive switching behaviors of ZnO. *Applied Physics Letters* **2011**, *99*, doi:10.1063/1.3659296.
51. Abdulrahman, A.F. The effect of different substrate-inclined angles on the characteristic properties of ZnO nanorods for UV photodetectors applications. *Journal of Materials Science: Materials in Electronics* **2020**, *31*, 14357-14374, doi:10.1007/s10854-020-03995-3.
52. Liao, Z.-M.; Xu, J.; Zhang, J.-M.; Yu, D.-P. Photovoltaic effect and charge storage in single ZnO nanowires. *Applied Physics Letters* **2008**, *93*, doi:10.1063/1.2957470.
53. Harnack, O.; Pacholski, C.; Weller, H.; Yasuda, A.; Wessels, J.M. Rectifying Behavior of Electrically Aligned ZnO Nanorods. *Nano Letters* **2003**, *3*, 1097-1101, doi:10.1021/nl034240z.
54. Fang, H.; Hu, W. Photogating in Low Dimensional Photodetectors. *Advanced Science* **2017**, *4*, 1700323, doi:https://doi.org/10.1002/advs.201700323.
55. Saxena, R.S. Study on Photoconductivity in Air and Vacuum of ZnO Prepared by different materials. *International Journal for Research in Applied Science and Engineering Technology* **2018**, *6*, 2466-2471.
56. Kushwaha, A.; Aslam, M. Defect induced high photocurrent in solution grown vertically aligned ZnO nanowire array films. *Journal of Applied Physics* **2012**, *112*, doi:10.1063/1.4749808.
57. Hullavarad, S.; Hullavarad, N.; Look, D.; Claflin, B. Persistent Photoconductivity Studies in Nanostructured ZnO UV Sensors. *Nanoscale Research Letters* **2009**, *4*, 1421, doi:10.1007/s11671-009-9414-7.
58. Komatsu, H.; Kawamoto, Y.; Ikuno, T. Freestanding Translucent ZnO–Cellulose Nanocomposite Films for Ultraviolet Sensor Applications. *Nanomaterials* **2022**, *12*, 940.
59. Ji, L.W.; Peng, S.M.; Su, Y.K.; Young, S.J.; Wu, C.Z.; Cheng, W.B. Ultraviolet photodetectors based on selectively grown ZnO nanorod arrays. *Applied Physics Letters* **2009**, *94*, doi:10.1063/1.3141447.
60. Pandey, S.; Shukla, A.; Tripathi, A. Highly sensitive and self powered ultraviolet photo detector based on ZnO nanorods coated with TiO2. *Sensors and Actuators A: Physical* **2023**, *350*, 114112, doi:https://doi.org/10.1016/j.sna.2022.114112.
61. Lin, Y.; Zou, J.; Wang, W.; Liu, X.; Gao, J.; Lu, Z. High-performance self-powered ultraviolet photodetector based on PEDOT:PSS/CuO/ZnO nanorod array sandwich structure. *Applied Surface Science* **2022**, *599*, 153956, doi:https://doi.org/10.1016/j.apsusc.2022.153956.
62. Shaikh, S.K.; Ganbavale, V.V.; Mohite, S.V.; Patil, U.M.; Rajpure, K.Y. ZnO nanorod based highly selective visible blind ultra-violet photodetector and highly sensitive NO2 gas sensor. *Superlattices and Microstructures* **2018**, *120*, 170-186, doi:https://doi.org/10.1016/j.spmi.2018.05.021.
63. Shang, S.; Dong, Y.; Zhang, W.; Ren, W. Fabrication and Performance of UV Photodetector of ZnO Nanorods Decorated with Al Nanoparticles. *Nanomaterials* **2022**, *12*, 3768.
64. Liu, N.; Fang, G.; Zeng, W.; Zhou, H.; Cheng, F.; Zheng, Q.; Yuan, L.; Zou, X.; Zhao, X. Direct Growth of Lateral ZnO Nanorod UV Photodetectors with Schottky Contact by a Single-Step Hydrothermal Reaction. *ACS Applied Materials & Interfaces* **2010**, *2*, 1973-1979, doi:10.1021/am100277q.
65. Cossuet, T.; Donatini, F.; Lord, A.M.; Appert, E.; Pernot, J.; Consonni, V. Polarity-Dependent High Electrical Conductivity of ZnO Nanorods and Its Relation to Hydrogen. *The Journal of Physical Chemistry C* **2018**, *122*, 22767-22775, doi:10.1021/acs.jpcc.8b07388.